ARTICLE IN PRESS

Nature Communications

https://doi.org/10.1038/s41467-026-68546-6

Article in Press

Ultrafast scintillating metal-organic framework films

Received: 10 August 2025

Accepted: 9 January 2026

[redacted]

Cite this article as: Dhamo, L., Perego, J., Villa, I. *et al.* Ultrafast scintillating metal-organic framework films. *Nat Commun* (2026). https://doi.org/10.1038/s41467-026-68546-6

Lorena Dhamo, Jacopo Perego, Irene Villa, Charl X. Bezuidenhout, Ilaria Mattei, Alessia Landella, Silvia Bracco, Angiolina Comotti & Angelo Monguzzi

We are providing an unedited version of this manuscript to give early access to its findings. Before final publication, the manuscript will undergo further editing. Please note there may be errors present which affect the content, and all legal disclaimers apply.

If this paper is publishing under a Transparent Peer Review model then Peer Review reports will publish with the final article.

ARTICLE IN PRESS

© The Author(s) 2026. **Open Access** This article is licensed under a Creative Commons Attribution-NonCommercial-NoDerivatives 4.0 International License, which permits any non-commercial use, sharing, distribution and reproduction in any medium or format, as long as you give appropriate credit to the original author(s) and the source, provide a link to the Creative Commons licence, and indicate if you modified the licensed material. You do not have permission under this licence to share adapted material derived from this article or parts of it. The images or other third party material in this article are included in the article's Creative Commons licence, unless indicated otherwise in a credit line to the material. If material is not included in the article's Creative Commons licence and your intended use is not permitted by statutory regulation or exceeds the permitted use, you will need to obtain permission directly from the copyright holder. To view a copy of this licence, visit http://creativecommons.org/licenses/by-nc-nd/4.0/.

Ultrafast scintillating metal-organic framework films.

Lorena Dhamo[1], Jacopo Perego[1†], Irene Villa[1†], Charl X. Bezuidenhout[1†], Ilaria Mattei[2], Alessia Landella[1], Silvia Bracco[1], Angiolina Comotti[1]* and Angelo Monguzzi[1]*

[1]Dipartimento di Scienza dei Materiali, Università degli Studi Milano-Bicocca, via R. Cozzi 55, Milano 20125, Italy

[2] INFN, Sezione di Milano, via G. Celoria 16, Milano 20133, Italy

[†] These authors equally contributed

Abstract.

Compositionally engineered metal-organic frameworks are designed and used to fabricate ultrafast scintillating films. The inclusion of hafnium ions in the nodes of the metal-organic framework enhances the interaction with ionizing radiation, partially compensating for the low density of the porous material and increasing the scintillation yield. The high diffusivity of molecular excitons within the framed conjugated ligands allows bimolecular annihilation processes that partially quench the system luminescence, resulting in fast scintillation pulses in the hundreds of picoseconds time scale. Despite the quenching, the gain in scintillation yield achieved is large enough to maintain the film light yield above 10^4 ph MeV^{-1} under soft X-rays. These high efficiencies and fast emission kinetics are obtained at room temperature in a technologically attractive solid-state configuration, placing the metal-organic framework platform in a prominent position for the realization of the next generation of fast scintillation counters for high-energy physics studies and medical imaging applications.

Corresponding authors:

Prof. Angiolina Comotti angiolina.comotti@unimib.it

Prof. Angelo Monguzzi angelo.monguzi@unimib.it

Introduction

Scintillation counters consist of a scintillating material, which is able to produce a light pulse upon interaction with ionizing radiations or particles, coupled to a photodetector, able to transduce the optical signal in an electrical output count.[1] Ultrafast efficient scintillators are now actively searched for several modern advanced applications where the detection of ionizing radiation and particles must be performed in an extremely short time with a good signal-to-noise ratio.[2] This is the case of forefront high-energy physics experiments, where extremely high event rates are generated and must be recorded avoiding pile up.[3] Additionally, faster detectors are also desirable when high quality images at low radiation flux are acquired for medical applications such as the time-of-flight positron emission tomography (ToF-PET) cancer imaging technique, which requests tens of picoseconds of time resolution in the detection of the γ-rays emitted by patients' injected radiotracers.[4,5]

The realization of luminous ultrafast scintillators with tens of picosecond reaction speed is therefore strongly desired, but it is a highly demanding challenge. Indeed, many parameters dominate the yield and kinetics of the scintillation mechanism, and they are usually anti-correlated. The material chemical composition, structure, intra- and intermolecular interactions, crystal symmetry, atomic number Z, electronic and charge transport properties, emission yield and light transport characteristics as well as the device geometry and size, all of them affect the complex photophysics beyond the scintillation mechanism and ultimately set the intensity and speed of the emitted scintillation light pulse. Currently, materials that show proper control on all the required parameters do not exhibit good light output and ultrafast emission kinetics at room temperature. Neither bulk and nanostructured crystalline inorganic scintillators, nor organic chromophores and plastics have the required characteristics at once. Materials with fast prompt luminescence, such as Cherenkov emission, would be promising if not for their low light yield (LY, the number of photons produced for each MeV of deposited energy), preventing them from achieving reasonable output intensity. Semiconductor nanocrystals and other high atomic-number nanomaterials are now considered, especially when embedded into polymeric matrices.[1,6-10] However, their implementation is difficult owing to the low stopping power of polymeric composites, dramatic emission self-absorption and the need for peculiar surface chemistry to optimize emission and chemical stability in the matrix. Recently proposed radical scintillators based on metal quantum clusters show an appropriate density and luminosity, but still they do not own adequate fast emission.[11-14] Conjugated systems can have a reasonably fast scintillation kinetics in the nanosecond time scale,[15-17] but inadequate stopping power for high-energy photons due to their low density.[18,19] In this regard, the use of a multicomponent heterostructured scintillator can to overcome the issues of traditional single component systems. A multicomponent heterostructured scintillator can be realized by coupling sheets of dense scintillating crystals such as bismuth germanate ($Bi_4Ge_3O_{12}$, BGO) to layers made of fast-emitting low density scintillators.[19-21] The dense block stops the 511 keV γ-rays by the photoelectric effect enabling a proper selection of events generated by the photons emitted by the ToF-PET radiotracer in the patient body. On the other hand, the fast emission is activated directly, in a minor way because of the weak interaction of γ-rays with the light material, and by the diffusing recoil photoelectrons generated in the dense scintillator that reach the fast emitting component. This latter mechanism of energy sharing is the main activation pathway for the fast emission of the system and it is actually considered one of the best strategy to obtain simultaneously energy resolution and timing performance.

Engineered luminescent metal-organic frameworks (MOFs), nanoporous hybrid materials consisting of a crystalline framework of conjugated fluorescent ligands linked to metal-oxide cluster nodes (Fig.1),[22-27] exhibit fast and efficient luminescence properties. Specifically, these hybrid materials have been recently proposed as scintillators,[28-34] since they contain both high-Z elements and highly emissive conjugated ligands. Indeed, we demonstrated the unique radiosensitization effect of the MOF architecture, which enhances the scintillation yield by enabling a better harvesting and down-conversion into radiative states of the deposited energy.[35] The use of MOFs has several intrinsic advantages: the MOFs' emission spectrum can be tailored and tuned by ultrafast energy transfer processes through the ligand framework to obtain a huge Stokes shift, avoiding reabsorption and maximizing light output;[36-39] the composition of MOF linking nodes can be ameliorated to include heavier elements to enhance primary interactions with γ-rays and high-energy secondary electrons. Moreover, the controlled growth of MOF thin films[40-43] recently allowed the fabrication of sensors based on different transduction mechanisms, ultra-selective membranes and photo- and electro-catalysts.[40,44-46]

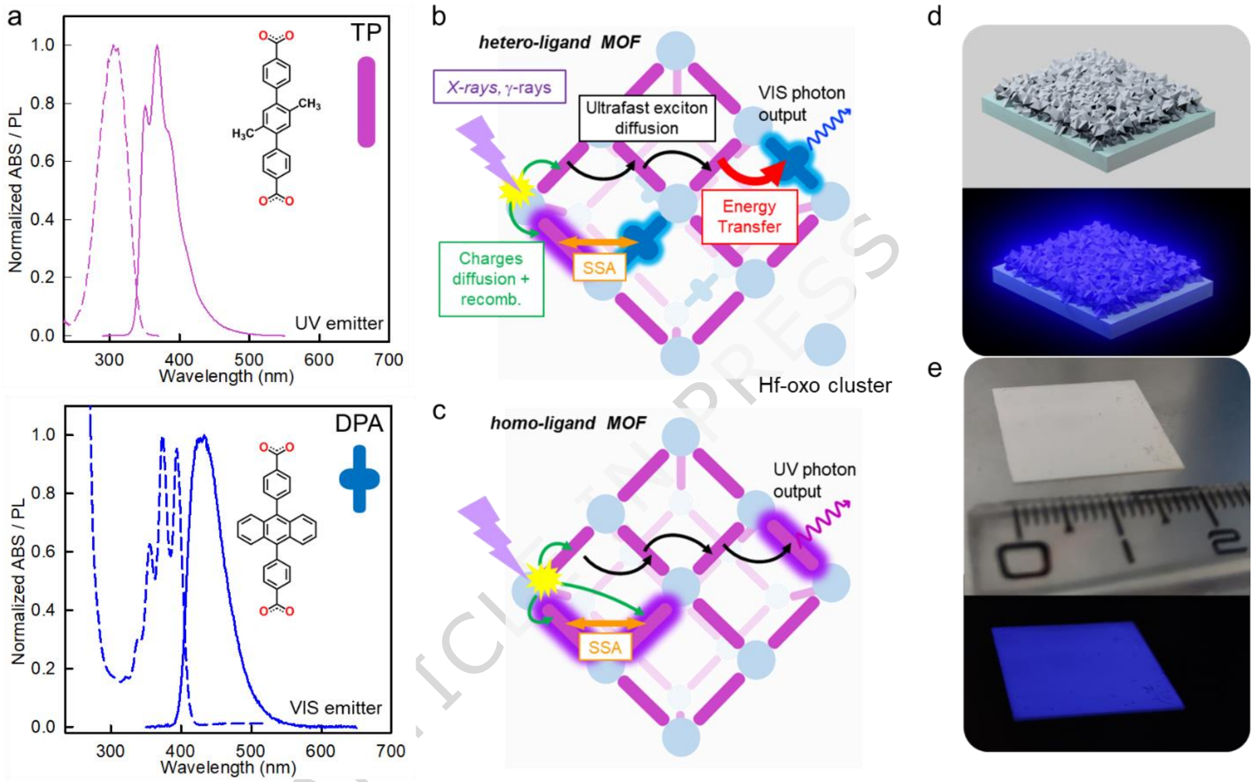

Figure 1 | Ligand properties and sketch of the photophysics involved in the MOFs scintillation. a, Normalized absorption (ABS, dashed lines) and photoluminescence (PL, solid lines) spectra of the conjugated ligands employed to assemble **b**, homo-ligand and **c**, hetero-ligand scintillating MOFs based on Hf-oxo-hydroxy clusters as linking nodes. Arrows indicate the ultrafast processes occurring in the framework of conjugated ligands during the scintillation mechanism, including singlet-singlet annihilation (SSA, double headed arrow) between excited ligands in the singlet state. **d**, Sketch of MOF films grown on a glass substrate under ambient lighting and UV light. **e**, Digital image of a 2×2 cm^2 glass substrate coated with a ca. 20 μm MOF film under ambient lighting and UV light.

Thus, MOF thin films hold great promise for realizing devices appealing for technological transfer as the fast emitters in scintillating metastructures and multicomponent devices. [19-21,47]

In this work, we obtain solid-state films of ultrafast-emitting MOFs, UV-emitting or with large Stokes shift blue emission, based on hafnium (Hf) oxo-hydroxy clusters as linking nodes (Hf-MOF). As conjugated scintillating ligands we use 2’,5’-dimethyl-[1,1’:4’,1’’-terphenyl]-4,4’’-dicarboxylate (TP), as energy donor or direct UV emitter in homo-ligand MOFs, and 4,4’-(anthracene-9,10-diyl)dibenzoate (DPA) as energy acceptor and blue emitter in hetero-ligand MOFs (Fig.1a). These MOF films feature a sub-nanosecond scintillation kinetics down to 150 ps and LY >10^4 ph MeV^{-1} under soft X-rays at room temperature, thus surpassing most state-of-the-art and commercially available fast scintillators. Photophysical investigations show that the crystalline MOFs play a pivotal role in preserving the individual ligand electronic and emission properties in a controlled arrangement and at short distances (<1 nm). This simultaneously allows for ultrafast diffusion-mediated bimolecular processes, such as energy transfer and singlet-singlet annihilation (SSA) between molecular excitons, that set their final characteristics as scintillators (Fig. 1b,c). The obtained results demonstrate that the MOF platform is an ideal candidate to reach a breakthrough in the most advanced scintillation detector technology and applications.

Results

Preparation and characterization of MOF powders and films. Luminescent Hf-MOF powders were prepared by a solvothermal process.[48,49] The homo-ligand MOF (denoted Hf-TP) was prepared using $HfCl_4$, benzoic acid (BA) as modulator, along with the linear, ditopic conjugated ligand, 2’,5’-dimethyl-[1,1’:4’,1’’-terphenyl]-4,4’’-dicarboxylate (TP), as a direct UV emitter. The blue-emissive hetero-ligand MOF was obtained by the co-assembly of TP ligand with a low percentage of 4,4’-(anthracene-9,10-dial)dibenzoate (DPA), promoting effective energy transfer and increasing the Stokes shift.[50] The MOFs were activated by thermal treatment at 110 °C under high vacuum and their composition was determined from ^1H solution NMR of the digested samples. In the hetero-ligand MOF a 1.6% molar fraction of DPA ligand was estimated (denoted Hf-DPA:TP-1.6%), and for both samples, the presence of BA was quantified to be 7-10% (Supplementary Figs. 1-3, Supplementary Tables 1-4). Infrared spectra of the MOFs displayed a peak at 1,600 cm^{-1} and a strong signal at 1,412 cm^{-1} associated with the asymmetric and symmetric stretching of the carboxylate coordinated to the Hf^{4+} ions (Supplementary Fig. 4). The crystal structures were elucidated from powder X-ray diffraction data using DFT methods and Rietveld refinement (Methods, Supplementary Figs. 5, 6, Supplementary Table 5). The Hf-MOFs crystallize in the cubic space group $Fm\text{-}3m$ and show short center-to-center ($d_{c\text{-}c}$) and phenyl-to-phenyl ($d_{Ph\text{-}Ph}$) distances between the ligands of 11.6 Å and 7.3 Å, respectively, which promote efficient energy diffusion and transfer within the framework (Fig. 2a, b). ^{13}C CP MAS NMR spectra exhibited sharp resonances and a multiplicity of TP signals in agreement with the high symmetry of the unit cell (Fig. 2c, Supplementary Figs. 7-9). MOF crystals display well-defined octahedral morphology with a homogeneous particle size of 7.1±0.8 μm for Hf-TP and 6.5±1.2 μm for Hf-DPA:TP-1.6% (Supplementary Figs. 10-12). The MOF samples are highly stable up to 400 °C, as established by thermal gravimetric analysis, and the experimental residues are consistent with their compositions determined by NMR (Supplementary Fig.13)**.** The MOFs exhibit open porosity with high Brunauer-Emmett-Teller (BET) and Langmuir surface areas of 3,263 $m^2 g^{-1}$ and 3,599 $m^2 g^{-1}$ for Hf-TP and 3,213 $m^2 g^{-1}$ and 3,541 $m^2 g^{-1}$ for Hf- DPA:TP-1.6%, and pore volumes of 1.22 $cm^3 g^{-1}$ and 1.21 $cm^3 g^{-1}$, respectively, consistent with the crystal structures (Supplementary Figs. 14-17, Supplementary Tables 6-8). Transmission Electron Microscopy (TEM) image of Hf-DPA:TP-1.6% crystalline powder displays well-defined crystals with sharp edges of length ~ 6 μm (Fig. 2d). High magnification images show lattice fringes with interplanar spaces of 17.1 Å and 15.4 Å, in good agreement with the (11-1) and (200) families of planes (Fig. 2e, Supplementary Fig. 18).[51] The good crystallinity of the sample was confirmed by the image of lattice fringes across all the crystals (Supplementary Fig. 18).

Towards real applications, we fabricated MOF films on a glass substrate using a home-built deposition chamber under optimized solvothermal conditions (Supplementary Fig. 19). Homo-ligand MOF film (denoted Hf-TP film) and hetero-ligand MOF films (denoted Hf-DPA:TP-*x*% films) with increasing amounts of DPA with respect to TP were grown and activated at 110 °C. The compositions of digested Hf-MOF films were checked by ^1H NMR (Supplementary Figs. 20-24, Supplementary Tables 9-11), yielding DPA molar fractions of 0.9%, 1.2%, and 2.3% for the hetero-ligand MOF films and an amount of the monofunctional ligand of 35-47%, higher than that of the crystalline powders. Considering the number of carboxylate units of both di- and mono-functional ligands, the clusters of the metal nodes can be connected by at least 8 difunctional ligands (TP and DPA) out of 12 (>70% connectivity), preserving a high connectivity of the architecture (Supplementary Table 12). Infrared spectra of the MOF films were consistent with the bulk crystalline powders, confirming the coordination of carboxylate units to Hf ions (Supplementary Fig. 25). ^{13}C CP MAS NMR spectra displayed signal broadening in the activated films, indicating some local disorder due to the presence of mono-functional ligands (Fig. 2c, Supplementary Figs. 26–28). X-ray diffraction patterns of solvent-filled Hf-MOF films confirm the cubic *Fm*-3*m* crystal structure (Fig. 2b, Supplementary Figs. 29-34). In the activated films, the diffraction peaks broaden and shift toward higher 2-Theta values with respect to those in the powders, indicating a shrinkage of the structure, as demonstrated by Rietveld refinement (Supplementary Figs. 29, 30, Supplementary Table 13). Consequently, the center-to-center and the phenyl-to-phenyl distances between the ligands shorten to 11.0 – 9.8 Å and 6.9 – 6.1 Å, respectively (Supplementary Fig. 31). This behavior can be ascribed to the replacement of di-carboxylate ligands with mono-carboxylate modulator moieties, which allow for a slight rearrangement of the framework. The peak broadening was analyzed by Rietveld refinement using the double-Voigt approach, which yields a mean domain size of 9±2 nm and 13±2 nm for Hf-TP film (activated) and Hf-DPA:TP-2.3% film (activated), respectively (Supplementary Figs. 32, 33), suggesting the formation of crystalline nanodomains. Scanning electron microscopy images of the activated thin films showed well-defined, aggregated octahedral crystals with a mean size of 1.4±0.3 μm forming a continuous layer with an average thickness of ~22±0.3 μm (Fig. 2f, g and Supplementary Figs. 35-39). TEM images of Hf-DPA:TP-2.3% MOF film confirm a crystal size of ~ 1 μm (Fig. 2h, Supplementary Fig. 40). These crystals exhibit a mosaic microstructure containing nanodomains and dark boundaries, which can be attributed to areas of mass contrast, according to the literature.[52] Higher magnification images enabled highlighting an ordered structure within nanodomains (Fig. 2i, Supplementary Fig. 41). The X-rays absorption of the films has been measured with a dedicated custom made setup (Supplementary Section 6, Supplementary Fig. 42).

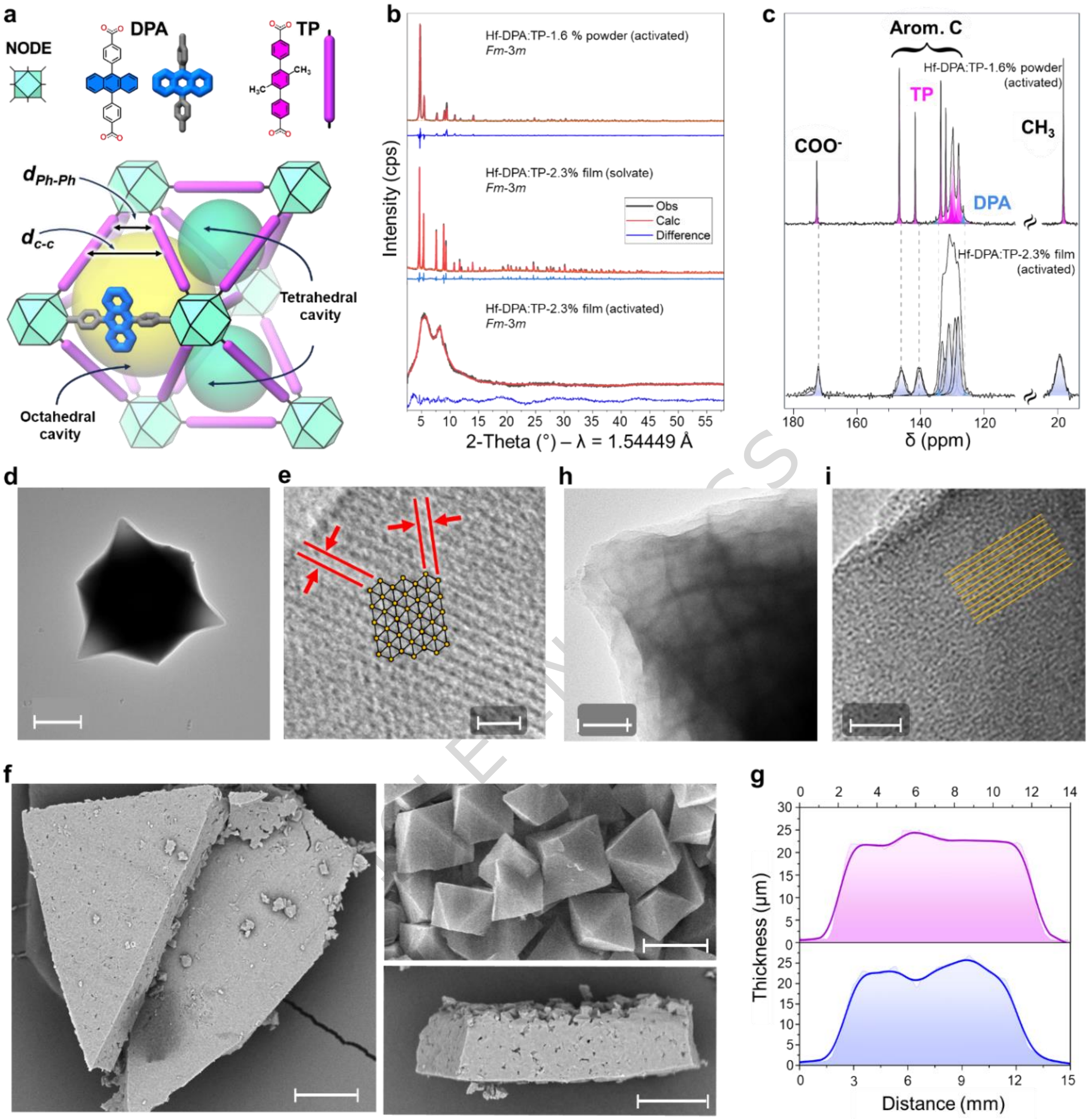

Figure 2 | Structural properties of hetero-ligand metal-organic framework (MOF) crystals and films. a, Hf-MOF composition and crystal structure highlighting the tetrahedral and octahedral cavities (green and yellow spheres, respectively) and the center-to-center ($d_{\text{c-c}}$) and phenyl-to-phenyl ($d_{\text{Ph-Ph}}$) distances between the ligands. **b**, X-rays diffraction (XRD) patterns and Rietveld plots of Hf-DPA:TP-1.6% powder (activated) and Hf-DPA:TP-2.3% films before and after activation. **c,** ^{13}C CP MAS NMR spectra of activated Hf-DPA:TP-1.6% powder (up) and the Hf-DPA:TP-2.3% film (down). **d**, **e**, Transmission Electron Microscopy (TEM) images of activated Hf-DPA:TP-1.6% powder at different magnifications. The (11-1) and (200) families of interplanar planes are highlighted. Scale bar is 2 µm and 5 nm in panel **d** and **e**, respectively. **f**, Scanning electron microscopy (SEM) images of activated Hf-DPA:TP-2.3% film deposited on glass substrate at different magnifications Scale bar in the left image and in the right bottom image is 25 µm. Scale bar in the right top image is 2 µm. **g**, Profilometry of the thickness of the Hf-TP (pink) and Hf-DPA:TP-2.3% (blue) films from side-to-side. **h-i**, TEM images of activated Hf-DPA:TP-2.3% film at different magnifications. Scale bar is 100 nm and 15 nm in panel **h** and **i**, respectively.

Luminescence and scintillation properties of MOF films. The luminescence properties of MOF powders and films have been investigated by means of steady-state and time-resolved photoluminescence and scintillation experiments. Figure 3a reports the photoluminescence spectra of the MOF powders under UV excitation at 250 nm. The crystalline powders of Hf-TP show the characteristic emission spectrum of the TP dye, with an emission characteristic lifetime of 236 ps (Supplementary Fig. 43). The Hf-TP:DPA-1.6% sample, thanks to the fast non-radiative energy transfer from TP ligands, shows the typical blue emission of DPA, with an emission characteristic lifetime of 1.8 ns (Supplementary Fig. 44). No UV luminescence is observed, thus demonstrating a complete TP-to-DPA energy transfer (Supplementary Fig. 45).[50,53] Hafnium has been chosen instead of the previously used zirconium[31] to enhance the absorption cross-section of high energy photons, which increases with a power law by following the atomic number Z of the interacting elements. This choice has several positive effects. First, the presence of Hf is crucial to provide the system with a reasonably good interaction probability with γ-rays. The simulated energy spectra reported in Fig. 3b show how hafnium (Z=72) dramatically increases the photoelectric-effect cross-section with 511 keV photons γ-rays employed in ToF-PET with respect to zirconium (Z=40). Here, the pulse height spectra of an ideal MOF bulk monolith (3×3×20 mm, density 0.77 g cm^{-3}, 2.3% DPA content, Supplementary Table 14) are compared to the ones of BGO (density 9.60 g cm^{-3}) and a standard polymer (density 1.00 g cm^{-3}) with the same size, as reference for dense and light scintillators, respectively. Notably, the Hf-based MOF shows a total fraction of photoelectric events of 7%, which is more than 10 times higher than that of the Zr-based MOF (0.5%), more than 30 times higher than the polymer (0.2%) and only 6 times lower than the high-density BGO (43.1%) used in ToF-PET scanners. This remarkable result suggests that Hf ions partially compensate for the low density of nanoporous MOFs. In addition, a more efficient high energy interaction with γ-rays means a more efficient energy deposition, affecting the LY of the scintillating material. As we recently demonstrated, the presence of the dense hafnium oxide clusters activates a local radiosensitization effect that enhances the low recombination yield of diffusing ionized charges, typical of low-density materials,[54-56] thus enhancing the system LY. The data reported in Fig. 3c show a clear increase of more than 300% in the LY of the MOF powders from Zr-based (Zr-DPA:TP-1.4%, ca. 3.6×10^{3} ph MeV^{-1})[50] to Hf-based systems (Hf-DPA:TP-1.6%, ca. 1.35×10^{4} ph MeV^{-1}) due to this effect. Importantly, the Hf-MOF films successfully retained emissive properties and energy transfer kinetics consistent with those observed in the powder MOF. Figure 3d shows the photoluminescence of the Hf-MOF film series with an increasing DPA amount ranging from 0.0%wt to 2.3%wt, at which concentration the energy transfer yield ϕ_{ET} from excited TP ligands to the DPA energy acceptors is ≥ 0.9 (Fig. 3d, Supplementary Fig. 45). Indeed, in MOFs based on conjugated ligands, the hopping-mediated diffusion of molecular excitons (Fig.1) is driven by Förster and Dexter non-radiative energy transfer mechanisms, with partial influence of phonons.[50] Specifically, in our MOFs, the emissive singlets move fast enough to experience energy transfer before radiative recombination, owing to their high diffusivity $D_{\mathrm{S}}^{\mathrm{TP}}$= 1.88×10^{-2} cm^{2} s^{-1} (lower limit value considering only on Förster interaction, Supplementary Information Section 4) within the framework facilitated by the high density of TP ligands. This allows the calculation of the energy transfer rate k_{ET} to DPA ligands in the rapid diffusion limit by

$$k_{\mathrm{ET}} = \frac{4\pi C_{\mathrm{DPA}} R_{\mathrm{Fs}}^{6} k_{\mathrm{TP}}}{3a^{3}}, \qquad (1)$$

where C_{DPA} is the DPA ligand concentration expressed in [cm^{-3}], R_{Fs} is the TP/DPA pair Förster radius, a is the minimum center-to-center distance between two molecular excitons in the frameworks and k_{TP} is the decay rate of the TP fluorescence in the absence of DPA (Supplementary Fig. 44).[57,58] The predicted energy transfer rate and yield $\phi_{\mathrm{ET}} = k_{\mathrm{ET}}/(k_{\mathrm{ET}} + k_{\mathrm{TP}})$ perfectly reproduce the experimental values measured as function of the DPA concentration (Supplementary Fig. 45), thus suggesting that TP-to -DPA energy transfer occurs in the tens-to hundreds of picosecond time regime with rates >> 1 GHz. Figure 3e shows the photoluminescence decay kinetics of Hf-DPA:TP-2.3% film recorded at 430 nm, i.e. at the peak of DPA emission, upon excitation at 340 nm in the DPA absorption band or at 250 nm in the TP absorption band. From both measurements a characteristic photoluminescence intensity decay time of ~ 2 ns was determined. No differences can be noted using different excitation energies, thus demonstrating that the activation of the large Stokes shift blue emission is unaffected by the TP-to-DPA energy transfer. The DPA emission intensity decays with a predominantly single exponential kinetics and a characteristic lifetime

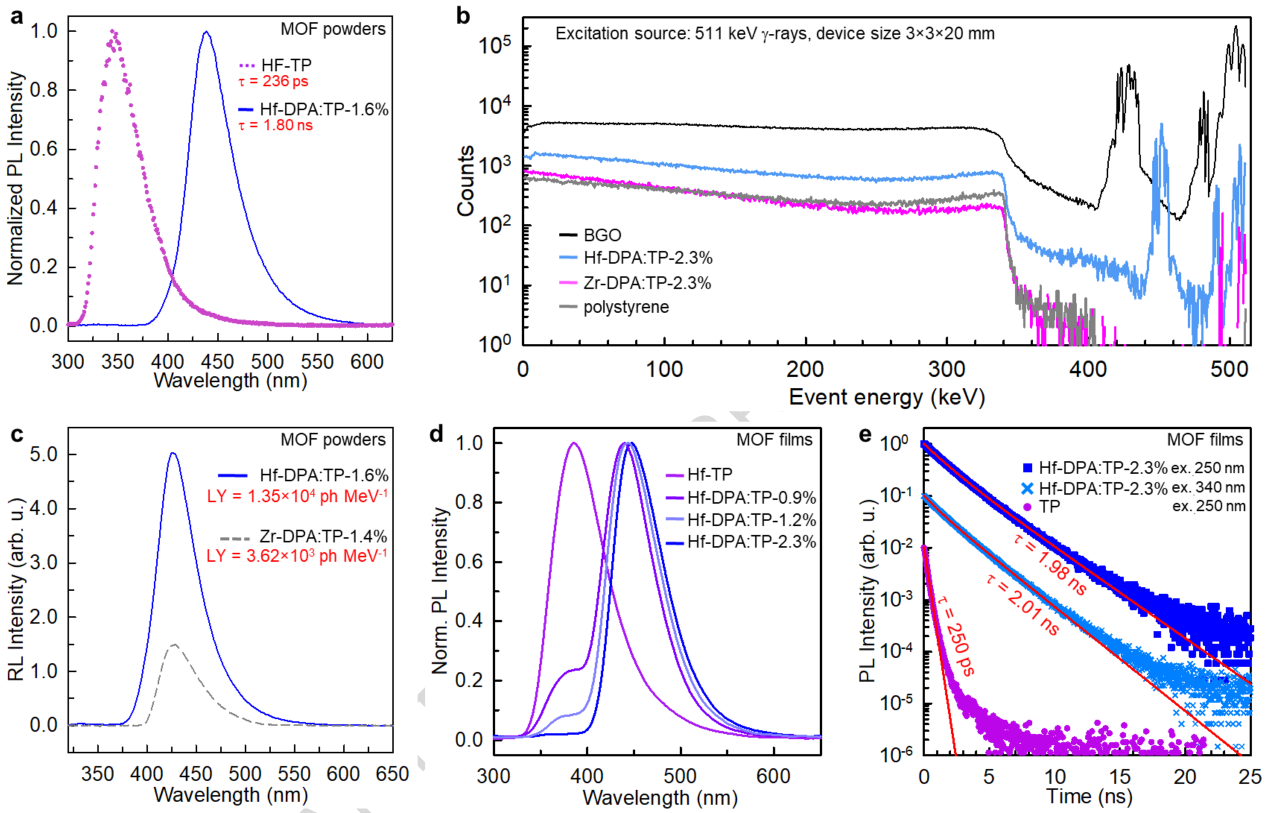

Figure 3 | Photoluminescence (PL) properties of homo- and hetero-ligand MOFs. a, PL spectra of Hf-DPA:TP-1.6% and Hf-TP crystalline powders under 250 nm excitation. **b,** Energy loss events probability calculated by a Monte Carlo method for 3×3×20 mm simulated monoliths of BGO, Hf-TP:DPA-2.3%, Zr-TP:DPA-2.3% and polystyrene for 511 keV photons. **c,** Radioluminescence (RL) spectra of Zr-DPA:TP-1.4% and Hf-DPA:TP-1.6% crystalline powders under soft X-rays. **d,** Normalized PL spectra of Hf-DPA:TP-*x*% films (22 μm) measured as function of the DPA content under 250 nm excitation. **e,** PL intensity decay vs. time for the Hf-DPA:TP-2.3% and Hf-TP films (22 μm) recorded at the PL peak under different laser excitation wavelengths.

similar to the powder (Fig. 3a, Supplementary Fig. 43). The same behavior is observed for the UV emitting homo-ligand Hf-TP film but with a faster characteristic lifetime of 250 ps (Fig.3c).

Figure 4a shows the radioluminescence spectrum of the Hf-TP and Hf-DPA:TP-2.3% films of 22 μm thickness (Fig. 2e) grown on a glass substrate (Supplementary Fig. 46) under soft X-ray excitation with an average energy of 7 keV. The radioluminescence of the films can be clearly observed with a total absorbed/delivered dose as low as 280 μGy/4 mGy (Supplementary Fig. 47, Supplementary Table 18). The films show the expected blue and UV luminescence bands matching the DPA and TP emission spectra, respectively, with a corresponding light yield of 1.19×10^4 ph MeV^{-1} and 1.28×10^4 ph MeV^{-1}. The associated estimated uncertainty is ±10%. These values have been measured with relative methods and directly measuring the energy deposited in the films by X-rays (Supplementary Information Section 6), in order to point out the intrinsic efficiency of the energy-to-photons conversion of the films, i.e. their LY . These results demonstrate that the energy transfer exploited to achieve the Stokes shift does not affect the film scintillation properties. Indeed, time-resolved scintillation experiments performed on MOF films as a function of the DPA concentration confirm the rapid diffusion kinetics of the energy transfer during scintillation (Supplementary Fig. 45). Figure 4b shows the intensity time decay kinetics of the TP scintillation at 340 nm recorded under pulsed X-rays at 14.5 keV as a function of the DPA loading. The drastic acceleration of the emission recombination kinetics observed in the presence of DPA (Fig. 3e) mirrors the faster energy transfer at higher DPA loading levels and allows the calculation of the experimental transfer rate. Notably, for the most performing Hf-DPA:TP-2.3% film, the data

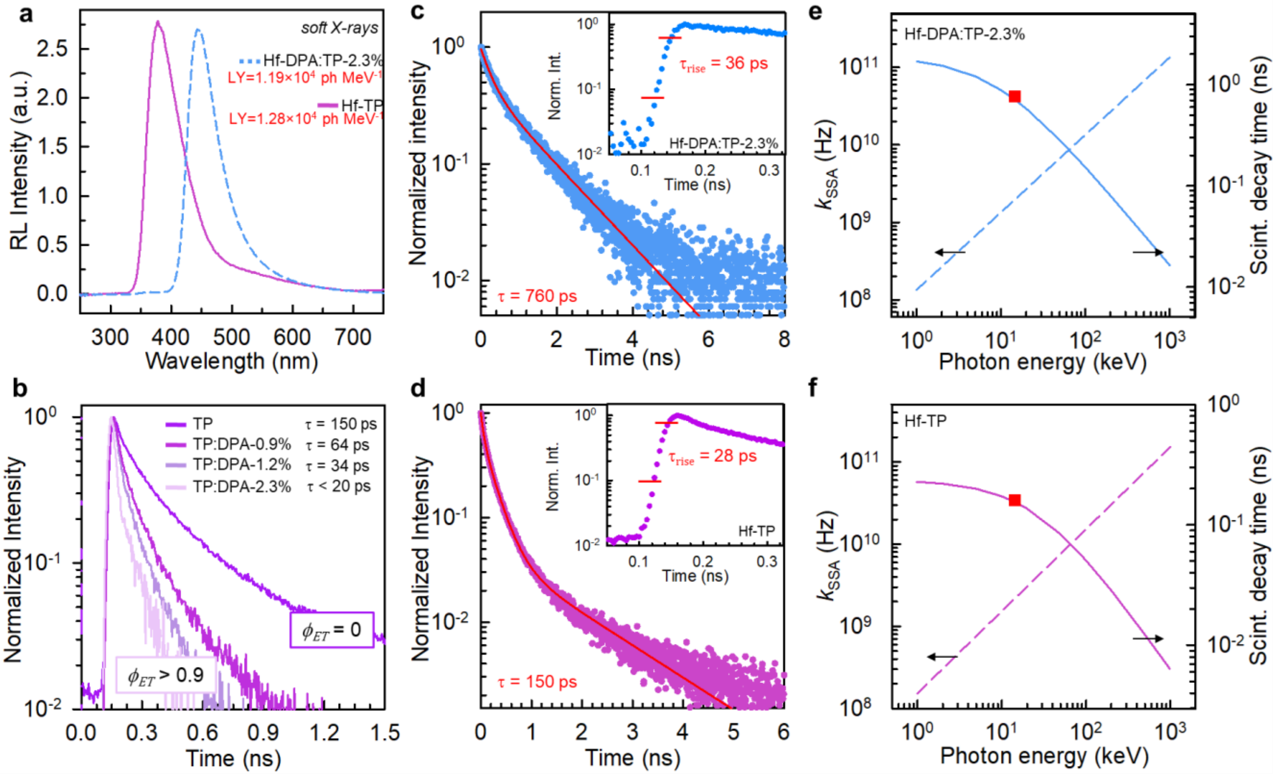

Figure 4 | Radioluminescence (RL) and scintillation properties of homo- and hetero-ligand MOFs. a, RL spectra of Hf-TP and Hf-DPA:TP-2.3% films (22 μm) under soft X-rays. **b**, Scintillation pulses under soft X-rays recorded at 340 nm in hetero-ligand MOF films as a function of the DPA amount. **c, d**. Scintillation pulses for Hf-DPA:TP-2.3% (c) and Hf-TP (d) MOF films recorded at 340 nm and 430 nm, respectively. **e, f**. Theoretical singlet-singlet annihilation (SSA) rate (dashed line) and scintillation lifetime (solid line) as a function of the incident photon energy. The red squares mark the experimental lifetime values reported, derived from the data in panels c and d.

indicate an energy transfer rate k_{ET} > 50 GHz (transfer time < 20 ps), as expected much faster than the approximated estimated value and below the instrumental resolution. The scintillation pulses recorded in the Hf-MOF films under pulsed X-rays show, in both cases, an excellent time response. The Hf-DPA:TP-2.3% scintillation (Fig. 4c) shows a rise time τ_{rise} = 36 ps and an average decay time τ = 760 ps, much faster than the photoluminescence lifetime. The Hf-TP film pulse (Fig. 4d) is quicker, with a faster rise time of 28 ps and a faster decay time of 150 ps, this latter again significantly shorter than the corresponding photoluminescence (Fig. 3e). Importantly, ultrafast kinetics and high LY are achieved at room temperature, surpassing any organic/polymeric scintillator and most of the recently proposed hybrid systems such as perovskites.[59-63]

The fast kinetics of the rise time is compatible with the exciton diffusivity within the ligands in Hf-TP, whilst in the hetero-ligand MOF it is slightly slower due to the picosecond-fast energy transfer step that activates DPA ligands. Specifically, the slowdown of the scintillation rise time points out an energy transfer speed of about 8 ps, corresponding to a rate of 12.5 THz, in agreement with the data reported in Fig. 4b. Moreover, the ultra-fast scintillation decay under pulse X-ray excitation hints at the presence of competitive biomolecular processes occurring in the MOF, even at low temperatures. If the diffusivity of singlets and their density are high enough, there could be a non-zero probability that two fluorescent singlets encounter and collide during their lifetime. The inelastic singlet-singlet annihilation (SSA) can therefore be a competitive channel to the singlet radiative recombination,[64] thus pushing to a faster recombination kinetics owing to a partial quenching of the excited singlet population. Figure 4e shows the rate k_{SSA} for hetero-molecular SSA (dashed line) in the Hf-DPA:TP-2.3% film calculated in the rapid diffusion limit by

$$k_{\mathrm{SSA}} = 4\pi\left(D_{\mathrm{S}}^{\mathrm{TP}} + D_{\mathrm{S}}^{\mathrm{DPA}}\right)R_{\mathrm{SSA}}[S_{\mathrm{DPA}}^{*}]\ , \tag{2}$$

as function of the energy of the incident photon from 1 to 10^3 keV (Supplementary Information Section 5). Specifically, $[S_{\mathrm{DPA}}^{*}]$ is the density of DPA singlets that can annihilate with the remaining diffusion TP singlets after energy transfer, a process possible since the DPA lifetime is much longer than the TP one. The $[S_{\mathrm{DPA}}^{*}]$ value is estimated as a function of the excitation photon energy by considering a full energy deposition by photoelectric events. R_{SSA} is the singlet-singlet annihilation distance, taken as large as a typical 2 nm to represent the collision of the two exciton molecular electronic orbitals.[65,66] Considering the energy difference between DPA emission and TP absorption that avoids back energy transfer, the diffusivity $D_{\mathrm{S}}^{\mathrm{DPA}}$ is considered equal to zero. Notably, the observed scintillation lifetime of 760 ps (red square) is in very good agreement with the predicted value of $\bar{\tau}_{\mathrm{scint}}^{\mathrm{DPA}} = (k_{\mathrm{scint}}^{\mathrm{DPA}})^{-1} = (k_{\mathrm{pl}}^{\mathrm{DPA}} + k_{\mathrm{SSA}})^{-1}$ where k_{SSA} is the SSA rate calculated considering the X-ray energy of 14.5 keV employed in the experiment (solid line). This modeling also reproduces the scintillation kinetics of the homo-ligand MOF. In this case the SSA rate is calculated as

$$k_{\mathrm{SSA}} = 8\pi D_{\mathrm{S}}^{\mathrm{TP}} R_{\mathrm{SSA}}[S_{\mathrm{TP}}^{*}], \tag{3}$$

where $[S_{\mathrm{TP}}^{*}]$ is now the density of generated TP singlets. Again, with photons at 14.5 keV, the predicted value of k_{SSA} allows the calculation of an expected scintillation lifetime $\bar{\tau}_{\mathrm{scint}}^{\mathrm{TP}}$ that matches the experimental value (Fig. 4f). This interpretation is corroborated by the following evidences. First, in agreement with the much less probable photoelectric interactions in the presence of Zr (Fig. 3b), the density of generated singlets in Zr-MOFs previously investigated is significantly lower than that in the Hf-MOFs considered here. Consequently, the SSA in Zr-MOFs is negligible and the scintillation lifetime matches that of the photoluminescence.[50] Second, the observed k_{SSA} rate in Hf-MOFs shows the expected fingerprint dependency on the energy of the excitation photons that changes the density of singlets (Supplementary Fig. 48). Indeed, at higher energies we observe a faster recombination kinetics, due to the more efficient SSA when a larger number of singlets are generated that quench more efficiently the MOF emission, in agreement with Eq. 2. Low temperature measurements further support that the scintillation behavior is dominated by exciton diffusion processes mainly based on electronic interactions (Supplementary Figs. 49-53).

To evaluate the potential of a new scintillator for fast timing applications, we can estimate the best temporal resolution achievable. Specifically, in the case of ToF-PET, a crucial figure of merit to be considered is the scanner coincidence time resolution (CTR), i.e. the minimum uncertainty on the detection time difference for the back γ-rays generated by the cancer radiotracer injected in the patient body. The intrinsic, all-optical CTR^0 value of a scintillator can be calculated by

$$\mathrm{CTR}^0 = 3.33\sqrt{\frac{\tau_{\mathrm{rise}}\,\tau_{\mathrm{eff}}}{N}} = 3.33\sqrt{\frac{\tau_{\mathrm{rise}}\,\tau_{\mathrm{eff}}}{\beta\chi E * \mathrm{LY}}}\ , \qquad (4)$$

where N is the total number of emitted photons, τ_{eff} is the effective scintillation decay time, β is the light outcoupling efficiency of the scintillator to the photodetector, E = 511 keV is the deposited energy by the γ-rays used in ToF-PET, and χ is the photodetector quantum efficiency at the scintillator emission wavelength.[19-21] Considering typical values of 0.3 and 0.25 for β and χ, respectively, we calculate a CTR^0 as low as 10 ps and 26 ps for Hf-TP and Hf-DPA:TP-2.3% films, respectively (Supplementary Information Section 7). In a model ToF-PET detection pixel with size 3×3×20 mm where photoelectric event distribution in space and the travelling path length distribution of the scintillation photons must be considered. These CTR^0 values translate into an estimated more realistic CTR of 30 ps and 50 ps for Hf-TP and Hf-DPA:TP-2.3% films, respectively, thus approaching the highly desired and extremely challenging 10 ps value for real-life devices.[5,67] Consequently, these results suggest that the ToF-PET time response using ultrafast scintillating MOFs will no longer be limited by the scintillation speed and yield, but just by the efficiency of employed photodetectors and light extraction. The technological appeal of MOF films is further supported by stability tests. After one year of exposure to air moisture, the investigated films show the same photoluminescence and radioluminescence properties (Supplementary Figs. 54-58). A limited emission efficiency loss of 15-20% is observed only under long-term exposure to high-power UV light or irradiating the sample with a high dose level of 70 Gy. Even after exposure to severe humid conditions (85% RH) for 3 days, the crystal structure is retained. The overall results clearly demonstrate the resistance of MOF films to harsh environmental and excitation conditions.

Discussion

In summary, by engineering the composition of Hf-based MOFs we were able to realize solid-state, ultrafast scintillating MOF films with emission both in the UV and the visible range, this latter thanks to a diffusion mediated energy transfer mechanism. The inclusion of high Z hafnium ions in the MOF linking nodes improves the material interaction cross-section with high energy photons partially compensating the low density of the framework, and significantly enhances their scintillation efficiency. Importantly, the crystalline framework, wherein molecular excitons move fast after the recombination of diffusing charges during scintillation, allows the occurrence of bimolecular quenching processes that set the kinetics to the shortest scintillation time achieved so far, down to 150 ps, for MOF based systems. Moreover, the gain in scintillation yield by the inclusion of Hf ions is high enough to keep the light yield of the films around 1.2×10^4 ph MeV^{-1}. This makes them the best performing fast emitting MOF-based scintillators at room temperature, overcoming most recent benchmark fast scintillators and commercial systems (Fig. 5 and Supporting Table 20). Thus, the proposed Hf-MOF films are excellent candidates to develop forefront fast ToF-PET detectors. The efficiency values, the ultrafast emission kinetics and the huge versatility of the MOF composition, that enables to design application-tailored systems and, potentially, control energy diffusion-mediated bimolecular process rates as well as their fabrication in the form of films, make MOF technologically-appealing candidates for the realization of next generation of ultrafast and high performance multicomponent scintillation counters.

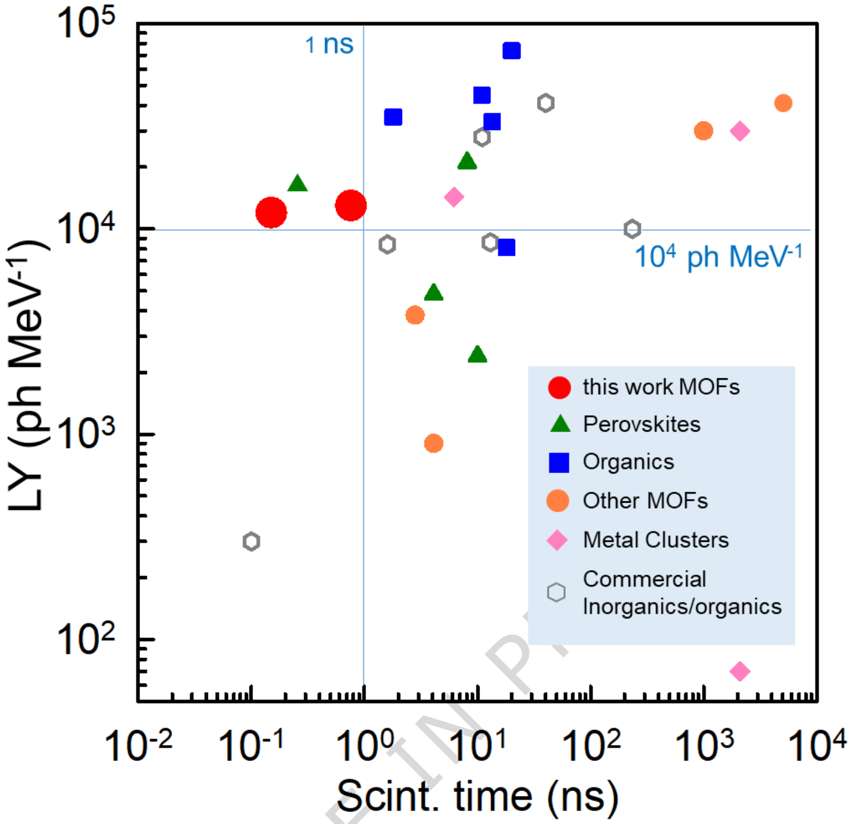

Figure 5 | State-of-the-art scintillators. Graphical summary of a performance comparison between state-of-the-art fast scintillating materials and the proposed MOF films at room temperature. Data details and relative source references are reported in the Supplementary Table 20.

Methods

Materials. Ligands 2′,5′-dimethyl-[1,1′:4′,1′′-Terphenyl]-4,4′′-dicarboxylic acid (TP) and 9,10-bis(4-carboxyphenyl)anthracene (DPA) were purchased from Fluorochem. Hafnium chloride (Cl_4Hf), benzoic acid (BA, 99.5%), hydrochloric acid (HCl), tetrahydrofuran (THF), dry dimethylformamide (DMF) and chloroform ($CHCl_3$) were purchased from Merck. Deuterated dimethyl sulfoxide (DMSO_d_6) and deuterated trifluoroacetic acid (TFA_d) were purchased from Merck.

Synthesis of Hf-TP and Hf-DPA:TP-x% powder. MOF nanocrystals were synthesized under solvothermal conditions modulated by benzoic acid. $HfCl_4$ was dispersed with 2’,5’-dimethyl-(1,1’:4’,1”-terphenil)-4,4”-dicarboxylic acid, benzoic acid and x% of 9,10-bis(4-carboxyphenyl) anthracene in DMF. The mixture was heated at 120°C for 20 h and the whitish powder obtained was collected and washed with fresh DMF and exchange with $CHCl_3$. The solvent was removed and the sample activated at 110°C for 18 h under high vacuum.

Synthesis of Hf-TP films. Homo-ligand MOF films were synthesized under solvothermal conditions modulated by benzoic acid. $HfCl_4$ was dispersed in DMF and sonicated for 15 minutes. The solution of $HfCl_2$ and DMF was added into the reactor containing 2’,5’-dimethyl-(1,1’:4’,1”-terphenil)-4,4”-dicarboxylic acid and benzoic acid and additional DMF. The reactor was sonicated for 5 minutes and the sample holder with a glass slip was inserted. The system was tightly sealed and heated at 120°C for 24h. The MOF-substrate was extracted, washed with fresh DMF and activated at 110°C for 18 h under high vacuum.

Synthesis of Hf-DPA:TP-x% films. Hetero-ligand MOF films were synthesized under solvothermal conditions modulated by benzoic acid. 9,10-bis(4-carboxyphenyl) anthracene was dispersed in DMF and heated up to 120°C for the complete dissolution of the ligand. Separately $HfCl_4$ was dispersed in DMF and sonicated for 15 minutes. The solution of $HfCl_2$ and DMF was added into the reactor containing 2’,5’-dimethyl-(1,1’:4’,1”-terphenil)-4,4”-dicarboxylic acid and benzoic acid and, lastly, the hot solution of DPA in DMF was poured. The reactor was sonicated for 5 minutes and the sample holder with a glass slip was inserted. The system is tightly sealed and heated at 120°C for 24 h. The MOF-substrate was extracted, washed with fresh DMF and activated at 110°C for 18 h under high vacuum.

The potential scalability of the MOF films fabrication has been preliminary tested several times and moving from 3×3×0.15 mm substrates to 10×10×0.15 mm and then 20×20×0.15 mm size substrates. All films show the same structural and emission properties.

Powder X-ray diffraction (PXRD). PXRD patterns were performed before and after the activation of the samples in a Rigaku SmartLab powder_diffractometer using Cu-Kα radiation, 40 kV, 30 mA over a range for 2θ of 2.0 - 70.0° with a step size of 0.02° and a scan speed of $1.0°\cdot min^{-1}$ equipped with a vacuum chamber (Anton Paar TTK 600) operating with liquid nitrogen cooling system. PXRD patterns under vacuum were collected under dynamic vacuum ($p < 1\times10^{-2}$ mmHg) between 293 K and 383 K. PXRD patterns were also performed using a Miniflex diffractometer with Cu-Kα radiation, 40 kV, 20 mA over a range for 2θ of 2.0 - 60.0° with a step size of 0.02° and a scan speed of $1.0°\ min^{-1}$.

Rietveld Refinement. Rietveld structural refinements of the X-ray data were performed using the TOPAS-Academic64 V6 software package. The initial model was constructed from a previously solved hetero-ligand Zr-DPA:TP-*x*% MOF model by replacing the Zr with Hf. The rigid bodies were set up such that the oxide and hydroxide moieties could adjust their relative position on the metal node. We also accounted for reorientation of the carboxylates, phenyl ring, dimethyl phenyl ring and the anthracene moieties. The occupancies for the composition of the ligand site were set to account for benzoate, modulator (BA), TP and DPA. ^{1}H solution NMR determined the occupancies of the different species. The structure was modelled as a disordered system with a space group *Fm*-3*m* for the final Rietveld refinement. The background was fitted and refined using a Chebyshev polynomial with 20 coefficients in the PXRD trace range from 2° to 60° 2-Theta with baseline shift refinement. The Simple Axial Model accounted for the asymmetry in the peaks, especially at low 2-Theta values. The peaks were fitted using a PearsonVII PVII function. For the XRD of the layer-grown MOF, a three-phase refinement was used with the unit cells of each phase allowed to be refined. Additional corrections include March-Dollase preferred orientation corrections on the (1 1 1), (2 0 0) and (3 1 1) reflections.

Solution NMR Analysis. NMR spectra were obtained using a Bruker Avance Neo spectrometer operating at 9.4 T (400 MHz) at 25 °C. ^{1}H NMR chemical shifts (δ) were reported in ppm relative to the proton resonances resulting from incomplete deuteration of the NMR solvents. According to a literature method, the composition of the hetero-ligand MOFs was quantified from the analysis of ^{1}H NMR spectra.

Thermogravimetric analysis. Thermal Gravimetric Analysis (TGA) was performed using a Mettler Toledo Star System 1 equipped with a gas controller GC10. Samples were outgassed overnight at 100°C under high vacuum ($p \leq 3\times10^{-6}$ bar) to remove adsorbed species. The experiments were conducted by applying a thermal ramp from 30°C to 1,000°C and a scan rate of 10°C min^{-1} in dry air.

FT-IR spectroscopy. Fourier-transform infrared spectroscopy was performed using a Thermo Scientific Nicolet iS20 spectrometer equipped with a Smart iTX Accessory for ATR measurements. The spectra were collected using 128 scans with a resolution of 4 cm^{-1} between 525 cm^{-1} and 4,000 cm^{-1} on activated samples in air.

Gas sorption analysis. Before sorption analysis, the samples were activated at 100°C overnight to remove solvent from the pores under high vacuum ($p \leq 3\times10^{-6}$ bar). Adsorption experiments were performed using N_2 with a purity of 5.0 and the adsorption isotherms at 77 K were collected on a Micromeritics 3Flex Adsorption Analyzer equipped with micropore analysis ports. Low-temperature analysis at 77 K and 195 K were conducted using liquid nitrogen bath. The N_2 adsorption isotherms at 77 K were analysed using Flex software. BET and Langmuir surface area were calculated between 0.015 and 0.065 p/p°. The pore size distributions were calculated using the NLDFT theory and the HS-2D carbon slit pore model.

High-Resolution SEM. Scanning electron microscopy (SEM) images were collected using a Zeiss Gemini 500 microscope, operating at 5 kV and with a Thermo Fisher Phenom G6 SEM, operating at 10 kV. The microcrystalline powders were deposited on a conductive tape, dried under a high vacuum, and sputtered with gold before the analysis (10 nm, nominal thickness). Images were also collected with a Thermo Fisher Phenom G6 SEM, operating at 10 kV

Profilometry. The thickness of the samples was measured using a Dektak 8 Stylus Profiler (Veeco Instruments, Inc.) equipped with an N-Lite low force sensor with a computerized surface and an accuracy in the range of 0.20 microns. The samples were characterized using a 2.5-μm-radius tip with a recording speed of 0.150 mm s^{-1} and a loading force of 0.03 mg.

Solid state NMR. ^{13}C and ^{1}H solid-state NMR experiments were carried out at 75.5 and 300.1 MHz, respectively, with a Bruker Avance Neo instrument operating at a static field of 7.04 T equipped with a 4 mm double resonance MAS probe. ^{13}C ramped-amplitude Cross Polarization (CP) experiments were performed at room temperature at a spinning speed of 12.5 kHz using a recycle delay of 5 s and a contact time of 2 ms. The 90° pulse for the proton was 2.5 μs. Crystalline polyethylene was taken as an external reference at 32.8 ppm from TMS. Quantitative ^{1}H SPE MAS NMR spectra were performed at room temperature at a spinning speed of 12.5 kHz using a recycle delay of 20 s. The 90° pulse for the proton was 2.4 μs. The ^{1}H chemical shift was referenced with respect to adamantane.

Photoluminescence studies. Time scale time-resolved photoluminescence experiments had been performed by using as excitation source a pulsed laser LED at 340 nm (3.65 eV, EP-LED 340 Edinburgh Instruments, pulse width 120 ps) and a pulsed laser LED at 250 nm (4.95 eV, EP-LED 250 Edinburgh Instruments, pulse width 77 ps) coupled to a Horiba Horiba-Jobin Yvon Simphony monochromator and, as photodetector, to and a hybrid photomultiplier tube PMA Hybrid 07 (Picoquant GmbH) coupled to a 4 ps resolution Pico Harp 300 TCSPC module. A custom-made 5000M spectrofluorimeter (Horiba-Jobin Yvon) equipped with a TBX-04 photon counting detector (IBH Scotland) and a single grating monochromator was used for the photoluminescence spectra measurements within the 200–800 nm range.

Radioluminescence studies. The samples were excited by unfiltered X-ray irradiation using a Philips PW2274 X-ray tube, with a tungsten target, equipped with a beryllium window and operated at 20 kV. At this operating voltage, X-rays are produced by the Bremsstrahlung mechanism, superimposed to the L and M transition lines of tungsten due to the impact of electrons generated through a thermionic effect and accelerated onto the tungsten target. Cryogenic radioluminescence measurements are performed in the 10−320 K interval. Radioluminescence of powders has been recorded on powder samples of 1 mm thickness in an aluminum sample holder.

Scintillation studies. The scintillation light pulses had been recorded in time correlated single photon counting (TCSPC) mode under pulsed X-ray excitation. For this purpose, an X-ray Tube (XRT) N5084 of Hamamatsu was used, activated by a pulsed 405 nm laser (pulse width EP-LED 250 Edinburgh Instruments, pulse width 120 ps). The X-rays energy spectrum was a bremsstrahlung continuous spectrum extending up to 40 keV (as the operating voltage is 40 kV, pulse width 80 ps) with an additional pronounced peak ≈ 9 keV due to Tungsten L-characteristic X-ray photons. As photodetector, a hybrid photomultiplier tube PMA Hybrid 06 (Picoquant GmbH) coupled to a 4 ps resolution Pico Harp 300 TCSPC module was used.

Light yield measurements under soft X-rays. The MOF LY was measured by relative methods using the EJ276D polymeric scintillators as reference (LY = 8.6×10^3 ph MeV^{-1}, experimentally confirmed in a 1 mm thick sample by comparison with a 1 mm BGO crystal, LY = 1×10^4 ph MeV^{-1}). For powders, 1 mm thick samples have been employed in an aluminum sample holder. The EJ-276D has been grinded to powders in order to have a quantitative and accurate comparison. For films, the EJ-276D has been sliced down to a 100 μm thickness and 20×20 mm shape to match the MOF/glass heterostructure and finely scratched on the surface to mimic the MOF layer scattering. The LY has been evaluated by comparing the relative radioluminescence integrated intensity recorded with the same experimental conditions. Given the low thickness of the film samples, the radioluminescence intensities have been corrected by the effective absorption of the excitation X-rays beam. To do that, we measure the integrated radioluminescence emission of a 5 mm BGO crystal under the excitation beam (100% absorption at 7 keV) and we compare its emission intensity when the beam goes through our film samples before hitting the BGO. The relative decrease of the BGO emission intensity allows us to estimate the relative absorptance of the excitation beam by any film, thus enabling a proper correction of the recorded radioluminescence intensity and therefore a proper evaluation of the films (Supplementary Information Section 6)

Radiation/Matter Monte Carlo Simulation. In order to evaluate the stopping power of MOFs for 511 keV γ-rays, a Monte Carlo simulation of the multilayer and bulk scintillators had been performed by means of the FLUKA code.[68] The simulated scintillators have a size of 3×3×20 mm, and their composition in terms of atomic weights and density had been fully reproduced. The 511 keV photons isotropic source had been put at a distance of 0.5 cm from the scintillator surface. The simulation output had been analyzed on an event-by-event basis through dedicated user-routines developed on purpose.

Data availability

The data that support the plots within this paper and other findings of this study are available from the corresponding author upon request. The X-ray crystallographic coordinates for structures reported in this study have been deposited at the Cambridge Crystallographic Data Centre (CCDC), under deposition numbers 2517615, 2517616, 2517617 and 2517618. These data can be obtained free of charge from The Cambridge Crystallographic Data Centre via www.ccdc.cam.ac.uk/data_request/cif

Acknowledgements

We acknowledge financial support from the Italian Ministry of University (MUR) through grant no. PRIN 2020-SHERPA no. H45F2100343000, grant and grant MINERVA – LuMIminesceNt scintillating hEterostructures foR advanced medical imaging no. H25E22000490006, PRIN-2022 HYSTAR no. H53D23004720006 and PRIN-2022 SHINE no. H53D23004500006. The authors acknowledge the Milano-Bicocca Solar Energy Research Center (MIB-SOLAR) and Dr. Chiara Liliana Boldrini for providing the facility to perform profilometric analysis of samples using Stylus Profiler. We thank Dr. Francesca Cova at the Department of Materials Science University of Milano-Bicocca for the help in setting up X-rays absorption measurements.

Authors contribution

I.V., J.P., A.C. and A.M. conceived the project. I.V., L.D. and A.M. performed the photoluminescence, radioluminescence experiments. J.P., C.X.B., A.L., L.D. S.B. and A.C. designed, synthesized and characterized the MOFs. A.L., L.D. and J.P. developed the MOF film growth strategy. C.X.B. and S.B. and A.C. performed the crystalline structure analysis and NMR experiments. I.M. managed the radiation matter modeling and simulation. I.V and A.M. developed the modeling of scintillation in MOFs. A.C. and A.M. wrote the paper. J.P., I.V. and C.X.B. equally contributed (†). All of the authors agreed to all of the content of the manuscript, the author list and its order, and the author contribution statements. Any changes to the author list after submission will be subject to approval by all authors.

Competing interests

The authors declare no competing interests.

Additional information

Supplementary information. The online version contains The online version contains supplementary material

available at……

References

1 Hou, B. *et al.* Materials innovation and electrical engineering in X-ray detection. *Nat. Rev. Electr. Eng.* **1**, 639–655 (2024).
2 Dujardin, C. *et al.* Needs, trends, and advances in inorganic scintillators *IEEE Trans. Nucl. Sci.* **65**, 1977–1997 (2018).
3 Community, E. ECFA R&D detectors. *European Community for Future Accellerators* (2021).
4 Turtos, R. M., Gundacker, S., Auffray, E., Lecoq, P. Towards a metamaterial approach for fast timing in PET: experimental proof-of-concept. *Phys. Med. Biol.* **64**, 185018 (2019).
5 Lecoq, P. *et al.* Roadmap toward the 10 ps time-of-flight PET challenge. **65**, 21RM01 (2020).
6 Park, J. M., Kim, H. J., Hwang, Y. S., Kim, D. H. & Park, H. W. Scintillation properties of quantum-dot doped styrene based plastic scintillators. *J. Lumin.* **146**, 157–161 (2014).
7 Hajagos, T. J., Liu, C., Cherepy, N. J. & Pei, Q. High-Z sensitized plastic scintillators: a review. *Adv. Mater.* **30**, 1706956 (2018).
8 Gandini, M. *et al.* Efficient, fast and reabsorption-free perovskite nanocrystal-based sensitized plastic scintillators. *Nat. Nanotech.* **15**, 462–468 (2020).
9 Guzelturk, B. *et al.* Bright and durable scintillation from colloidal quantum shells. *Nat. Commun.* **15**, 4274 (2024).
10 Cova, F. *et al.* Scintillation properties of CsPbBr3 nanocrystals prepared by ligand-assisted reprecipitation and dual effect of polyacrylate encapsulation toward scalable ultrafast radiation detectors. *Nano Lett.* **24**, 905–913 (2024).
11 Yuan, J.-W. *et al.* Short Lifetime Radical Metal Cluster Scintillator. *Angew. Chem. Int. Ed.* **64**, e202503457 (2025).
12 Hu, Y.-S. *et al.* Temperature-Inert Coinage Metal Cluster Scintillator. *Angew. Chem. Int. Ed.* **64**, e202508552 (2025).
13 Han, B.-L. *et al.* Hydrogen-Bonding-Assisted Assembly of Stable High-Nuclearity Copper(I)-Alkyne Nanoclusters for X-Ray Scintillation. *Angew. Chem. Int. Ed.* **64**, e202507412 (2025).
14 Peng, Q.-C. *et al.* Thermally Activated Delayed Fluorescence Coinage Metal Cluster Scintillator. *ACS Cent. Sci.* **9**, 1419–1426 (2023).
15 Hamel, M. *Plastic Scintillators: Chemistry and Applications*. (Springer International Publishing, 2021).
16 Du, X. *et al.* Efficient and ultrafast organic scintillators by hot exciton manipulation. *Nat. Photon.* **18**, 162–169 (2024).
17 Exciton Luxxotica commercial scintillating dyes (https://exciton.luxottica.com/laser-dyes.html)
18 Orfano, M. *et al.* Fast Emitting Nanocomposites for High-Resolution ToF-PET Imaging Based on Multicomponent Scintillators. *Adv. Mater. Tech.* **9**, 2302075 (2024).
19 Sala, M. *et al.* Highly Luminous Scintillating Nanocomposites Enable Ultrafast Time Coincidence Resolution for γ-rays Detection with Heterostructured Multilayer Scintillators. *Adv. Funct. Mater.* 2421434 (2024).
20 Pagano, F. *et al.* Advances in heterostructured scintillators: toward a new generation of detectors for TOF-PET. *Phys. Med. Biol.* **67**, 135010 (2022).
21 Pagano, F. *et al.* Modeling scintillation kinetics and coincidence time resolution in heterostructured scintillators. *IEEE Trans. Nucl. Sci.* **70**, 2630–2637 (2023).
22 Yaghi, O. M. *et al.* Reticular synthesis and the design of new materials. *Nature* **423**, 705–714 (2003).
23 Lustig, W. P. *et al.* Metal–organic frameworks: functional luminescent and photonic materials for sensing applications. *Chem. Soc. Rev.* **46**, 3242–3285 (2017).
24 Ha, D.-G. *et al.* Exchange controlled triplet fusion in metal–organic frameworks. *Nat. Mater.* **21**, 1275–1281 (2022).
25 Kitagawa, S., Kitaura, R. & Noro, S. Functional porous coordination polymers. *Angew. Chem. Int. Ed.* **43**, 2334–2375 (2004).
26 Horike, S., Shimomura, S. & Kitagawa, S. Soft porous crystals. *Nat. Chem.* **1**, 695–704 (2009).

27 Furukawa, H., Cordova, K. E., O'Keeffe, M. & Yaghi, O. M. The chemistry and applications of metal-organic frameworks. *Science* **341**, 1230444 (2013).

28 Doty, F. P., Bauer, C. A., Skulan, A. J., Grant, P. G. & Allendorf, M. D. Scintillating Metal-Organic Frameworks: A New Class of Radiation Detection Materials. *Adv. Mater.* **21**, 95–101 (2009).

29 Wang, J.-X. *et al.* Nearly 100% energy transfer at the interface of metal-organic frameworks for X-ray imaging scintillators. *Matter* **5**, 253–265 (2022).

30 Mauree, S. *et al.* Detection of Radioactive Gas with Scintillating MOFs. **33**, 2302877 (2023).

31 Orfano, M. *et al.* Efficient radioactive gas detection by scintillating porous metal–organic frameworks. *Nat. Photon.* **17**, 672–678 (2023).

32 Chen, H. *et al.* Ultrabright and Water-Stable Eu(III)-Based MOF Scintillators Sensitized by Dual-Antenna Ligands for Real-Time and Underwater X-Ray Imaging. *Angew. Chem. Int. Ed.* **64**, e202506118 (2025).

33 Chen, B. *et al.* Radiation-Responsive Metal–Organic Frameworks: Fundamentals and Applications. *Adv. Funct. Mater.* **34**, 2310270 (2024).

34 Peng, Q.-C. *et al.* High Performance Dynamic X-ray Flexible Imaging Realized Using a Copper Iodide Cluster-Based MOF Microcrystal Scintillator. *Angew. Chem. Int. Ed.* **62**, e202308194 (2023).

35 Perego, J. *et al.* Composite fast scintillators based on high-Z fluorescent metal–organic framework nanocrystals. *Nat. Photon.* **15**, 393–400 (2021).

36 Jia, J. *et al.* Access to highly efficient energy transfer in metal–organic frameworks via mixed linkers approach. *J. Am. Chem. Soc.* **142**, 8580–8584 (2020).

37 Ren, D. *et al.* Tuning and directing energy transfer in the whole visible spectrum through linker installation in metal–organic frameworks. *Angew. Chem. Int. Ed.* **60**, 25048–25054 (2021).

38 Perego, J. *et al.* Highly luminescent scintillating hetero-ligand MOF nanocrystals with engineered Stokes shift for photonic applications. *Nat. Commun.* **13**, 3504 (2022).

39 Orfano, M. *et al.* Reabsorption-Free Scintillating Hetero-Ligand MOF Crystals Activated by Ultrafast Energy Transfer. *Adv. Funct. Mater.* **34**, 2404480 (2024).

40 Shekhah, O., Liu, J., Fischer, R. A. & Wöll, C. MOF thin films: existing and future applications. *Chem. Soc. Rev.* **40**, 1081–1106 (2011).

41 Gutiérrez, M., Martín, C., Van der Auweraer, M., Hofkens, J. & Tan, J. C. Electroluminescent guest@ MOF nanoparticles for thin film optoelectronics and solid-state lighting. *Adv. Opt. Mater.* **8**, 2000670 (2020).

42 Yu, X. *et al.* Ln-MOF-Based Hydrogel Films with Tunable Luminescence and Afterglow Behavior for Visual Detection of Ofloxacin and Anti-Counterfeiting Applications. *Adv. Mater.* **36**, 2311939 (2024).

43 Wang, J.-X., Shekhah, O., Bakr, O. M., Eddaoudi, M. & Mohammed, O. F. Energy transfer-based X-ray imaging scintillators. *Chem* **11** (2025).

44 Ellis, J. E., Crawford, S. E. & Kim, K.-J. Metal–organic framework thin films as versatile chemical sensing materials. *Mater. Adv.* **2**, 6169–6196 (2021).

45 Miner, E. M. *et al.* Electrochemical oxygen reduction catalysed by Ni3(hexaiminotriphenylene)2. *Nat. Commun.* **7**, 10942 (2016).

46 Cheng, Y. *et al.* Advances in metal–organic framework-based membranes. *Chem. Soc. Rev.* **51**, 8300–8350 (2022).

47 Kurman, Y. *et al.* Purcell-enhanced x-ray scintillation. *Sci. Adv.* **10**, eadq6325 (2024).

48 Schaate, A. *et al.* Modulated Synthesis of Zr-Based Metal–Organic Frameworks: From Nano to Single Crystals. *Chem.* **17**, 6643–6651 (2011).

49 Bai, Y. *et al.* Zr-based metal–organic frameworks: design, synthesis, structure, and applications. *Chem. Soc. Rev.* **45**, 2327–2367 (2016).

50 Orfano, M. *et al.* Reabsorption-Free Scintillating Hetero-Ligand MOF Crystals Activated by Ultrafast Energy Transfer. *Adv. Funct. Mater.* **34**, 2404480 (2024).

51 Johnstone, D. N. *et al.* Direct Imaging of Correlated Defect Nanodomains in a Metal–Organic Framework. *J. Am. Chem. Soc.* **142**, 13081–13089 (2020).

52 Cliffe, M. J. *et al.* Correlated defect nanoregions in a metal–organic framework. *Nat. Commun.***5**, 4176 (2014).

53 Lakowicz, J. R. *Principles of Fluorescence Spectroscopy*. (Kluwer Academic/Plenum, 1999).

54 Payne, S. A. *et al.* Nonproportionality of scintillator detectors: Theory and experiment. II. *IEEE Trans. Nucl. Sci.* **58**, 3392–3402 (2011).

55 Moses, W. *et al.* The origins of scintillator non-proportionality. *IEEE Trans. Nucl. Sci.* **59**, 2038–2044 (2012).

56 Villa, I. *et al.* On the Origin of the Light Yield Enhancement in Polymeric Composite Scintillators Loaded with Dense Nanoparticles. *Nano Lett.* **24**, 8248–8256 (2024).

57 Thomas, D. D., Carlsen, W. F. & Stryer, L. Fluorescence energy transfer in the rapid-diffusion limit. *Proc. Nat. Acad. Sci.* **75**, 5746–5750 (1978).

58 Stryer, L., Thomas, D. D. & Meares, C. F. Diffusion-enhanced fluorescence energy transfer. *Ann. Rev. Biophys. Bioeng.***11**, 203–222 (1982).

59 Turtos, R. M. *et al.* Ultrafast emission from colloidal nanocrystals under pulsed X-ray excitation. *J. Instr.* **11**, P10015 (2016).

60 Turtos, R. M., Gundacker, S., Omelkov, S., Auffray, E. & Lecoq, P. Light yield of scintillating nanocrystals under X-ray and electron excitation. *J. Lumin.* **215**, 116613 (2019).

61 Erroi, A. *et al.* Ultrafast and Radiation-Hard Lead Halide Perovskite Nanocomposite Scintillators. *ACS Energ. Lett.* **8**, 3883–3894 (2023).

62 Rutstrom, D. *et al.* New ultrafast scintillators with core valence luminescence: Cs2MgCl4 and Cs3MgCl5. *J. Mater. Chem. C* **12**, 6920–6931 (2024).

63 Zaffalon, M. L. *et al.* Ultrafast Superradiant Scintillation from Isolated Weakly Confined Perovskite Nanocrystals. *Adv. Mater.* **37**, 2500846 (2025).

64 Birks, J. B. *Photophysics of Aromatic Molecules*. (Wiley-Interscience, 1970).

65 Perrin, F. J. Comptes Rendu, Loi de decroissance du pouvoir fluorescent en fonction de la concentration. *Compt. Rend. Acad. Sci.* **178**, 1978 (1924).

66 Inokuti, M. & Hirayama, F. Influence of energy transfer by the exchange mechanism on donor luminescence. *J. Chem. Phys.* **43**, 1978–1989 (1965).

67 Lecoq, P. On the way to the 10 ps time-of-flight PET challenge. *Eur. Phys. J. Plus* **137**, 964 (2022).

68 Böhlen, T. T. *et al.* The FLUKA Code: Developments and Challenges for High Energy and Medical Applications. *Nucl. Dat. Sheet.* **120**, 211–214 (2014).

Editor's Summary

Dhamo et al. report metal-organic framework based X-ray scintillating films with hafnium oxide clusters as linking nodes and conjugated ligands as emitting centres. It reveals that the diffusion-mediated bimolecular processes lead to fast scintillation kinetics down to 150 ps and light yield over 10^4 ph MeV-1.

Peer review information: *Nature Communications* thanks Kai Li who co-reviewed with Qiu-Chen Peng; and the other anonymous reviewer(s) for their contribution to the peer review of this work. A peer review file is available.